Chemical Science

ROYAL SOCIETY OF CHEMISTRY

EDGE ARTICLE

View Article Online
View Journal | View Issue



Cite this: *Chem. Sci.*, 2025, **16**, 19328

All publication charges for this article have been paid for by the Royal Society of Chemistry



# Quantum sensing of paramagnetic analytes by nanodiamonds in levitated microdroplets and aqueous solutions

Emily K. Brown, [ab] Zachary R. Jones, [bc] Adrisha Sarkar,[b] Brandon J. Wallace, [ab] Ashok Ajoy*[ab] and Kevin R. Wilson *[a]

Nanodiamonds (ND) hosting negatively charged nitrogen-vacancy ($NV^-$) color centers have received attention for applications in magnetic field, electric field, chemical, and bio-sensing. The versatility of these probes is their excellent room-temperature optical and spin properties, along with their small size, functionalized surfaces and resistance to bleaching, making them ideal as nanoscopic sensors in picoliter volumes (*e.g.* single cells, but also microcompartments and aerosols). For quantitative ND-$NV^-$ sensing of paramagnetic analytes in such contexts, however, there remains an incomplete understanding of how factors related to the aqueous phase environment control detection efficiency. To address this, optically detected magnetic resonance (ODMR) is measured in bulk macroscale solutions and single levitated microdroplets as a function of $Gd^{+3}$ concentration (340 nM to 1.5 mM), nanodiamond size, pH, competitor ions, and ligands. The ODMR response to $[Gd^{+3}]$ is found to be nonlinear, and pH, ND and sample volume dependent; indicating the detection of $Gd^{+3}$ requires efficient adsorption of the analyte to the diamond surface. Langmuir adsorption isotherms embedded in a quantitative photophysical model links the ODMR response to adsorption thermodynamics of $Gd^{+3}$. The equilibrium constant for $Gd^{+3}$ adsorption to a carboxylated ND surface is determined to be $(1 \pm 0.5) \times 10^5$ $M^{-1}$ corresponding to a free energy of adsorption of $(-28 \pm 1)$ kJ $mol^{-1}$. These results provide general insight into how complex aqueous and microscale environments impact nanodiamond based quantum sensing modalities, and portend their application as quantitative chemical sensors in microenvironments.

Received 5th June 2025
Accepted 11th September 2025

DOI: 10.1039/d5sc04108b

rsc.li/chemical-science

## 1. Introduction

Microdroplets have emerged as unique environments that dramatically accelerate chemical reactions by many orders of magnitude compared to bulk macroscale solutions (*i.e.*, beakers). Reaction enhancement is proposed to involve pH gradients,[1] surface electric fields,[2–5] partial solvation,[6] reactant partitioning to the interface,[7] and spontaneous radical formation.[8,9] Testing of these proposed mechanisms is limited by the lack of *in situ* probes. Negatively charged nitrogen-vacancy ($NV^-$) centers in nanodiamonds (ND) are promising tools to measure chemical reactions in these microcompartments non-destructively and *in situ*. Their potential arises from their small size, resistance to photobleaching, chemical inertness, and the ability to functionalize the ND surface to target key analytes.[10] Optical readout of ND-$NV^-$ enables detection of magnetic[11] and electric fields,[12,13] and paramagnetic species,[14,15] with the additional possibility of deploying nanoscale EPR and NMR sensors[16–20] in microenvironments (*e.g.*, cells, aerosol and microdroplets) making them ideal probes of chemistry in small volumes.

We envision that $NV^-$ centers located in nanodiamonds could help to elucidate microdroplet chemistry; especially in the sensing of reactions involving radical species. Indeed, significant debate exists around claims of spontaneous radical formation in microdroplets, which these probes have the potential to resolve.[9,21,22] However, key challenges remain in correlating the ND-$NV^-$ optical response to quantitative analyte concentrations. For example, kinetic measurements of paramagnetic species are often not quantitative,[14,23] due to the inherent complexity of the sensing mechanism involving a solid surface or particle in contact with an aqueous solution. As shown previously,[24–26] there is evidence that low level detection of analytes by ND-$NV^-$ occurs *via* a two-step mechanism; where the paramagnetic analyte in solution diffuses to and adsorbs to a ND surface prior to detection. This process is governed by: (1) the thermodynamics of analyte adsorption to the solid–liquid interface and (2) the coupling of adsorbed surface spin to $NV^-$ center inside the nanodiamond lattice. It is expected that any

[a]*Chemical Sciences Division, Lawrence Berkeley National Laboratory, Berkeley, CA, 94720, USA. E-mail: ashokaj@berkeley.edu; krwilson@lbl.gov*

[b]*Department of Chemistry, University of California, Berkeley, CA 94720, USA*

[c]*Advanced Biofuels and Bioproducts Process Development Unit (ABPDU), Biological Systems and Engineering Division, Lawrence Berkeley National Laboratory, Berkeley, CA 94720, USA*

species in solution that either directly or indirectly enhances or suppresses adsorption of a paramagnetic species to the ND surface will have an impact on analyte quantification and detection sensitivity.

With the eventual aim of quantifying chemistry in microdroplets and microemulsions, in this paper, we investigate how pH, sample volume (*e.g.* droplet or bulk), nanodiamond size, shape, and co-solutes influence the adsorption/detection of $Gd^{+3}$. We use a model system comprised of $Gd^{+3}$ (with 7 unpaired spins) and carboxylated ND particles to understand how the aqueous phase environment might affect the sensing of paramagnetic species (*e.g.*, free radicals, $O_2$, metals) using optically detected magnetic resonance (ODMR). Experiments are performed in the bulk, and in single levitated microdroplets. A colliding droplet scheme, as illustrated in Fig. 1A, enables the self-referential ODMR measurement within the droplet, because of the ability to measure ODMR before and after the addition of $Gd^{+3}$. We quantitatively analyze these experimental results by embedding a Langmuir adsorption isotherm into a photophysical model of a ND-$NV^-$ to achieve a self-consistent description of $Gd^{+3}$ sensing in aqueous environments. More generally, these results offer better understanding of how the complex aqueous phase environment encountered in cells and microdroplets containing buffers, salts, metals, and ligands influence the detection of paramagnetic molecules and ions.

## 2. Experimental and theoretical methods

ND-$NV^-$ are deployed in the bulk aqueous solutions (*i.e.*, cuvette) and in single microdroplets levitated in a quadrupole trap (Fig. 1A) as detailed in Sections 2.1 and 2.2. The model framework used to interpret these measurements follows in Section 2.3.

### 2.1 Droplet measurements

Droplet experiments are performed in a branched quadrupole trap, which has been previously described[27–30] and illustrated in Fig. 1A. Individual droplets with an average radius of 17 μm are charged and levitated through electrostatic repulsion in the environmentally controlled quadrupole trap. To maintain droplet stability the relative humidity in the trap is held at 80 ± 3.5% by flowing nitrogen through a bubbler at a rate of 0.1 SLM. Droplets, formed by a piezoelectric dispenser (MicroFAB), are illuminated by a laser (Opto Engine, 532 nm), and their size, within ±0.5 μm, is obtained from the Mie scattering pattern recorded with a line camera (ThorLabs LC100) positioned at a 90° angle to the laser axis. A second positioning camera fixes the droplet location with respect to the microwave antenna to ensure that consistent microwave power is delivered to the droplet during and between experiments. Stable droplets are formed from 55% HPLC water (Sigma-Aldrich Lot SHBQ7126) and 45% glycerol (Sigma-Aldrich Lot SHBH9768), which corresponds to a water activity of 0.8 and matches the relative humidity in the trap described above.[31]

Carboxylated (–COOH) red fluorescent nanodiamonds (purchased from Adámas Nanotechnologies) with nominal average hydrodynamic diameters of 70, 100, 140, and 750 nm, and approximately 3 ppm NV centers, are used for all measurements. The average hydrodynamic diameters, size distributions and associated uncertainties are derived from dynamic light scattering (DLS) measurements assuming a spherical shape, as reported by Adámas Nanotechnologies.[32] For clarity, here we refer to the hydrodynamic diameter as the nominal diameter. Since the diamonds are highly non-spherical, the hydrodynamic

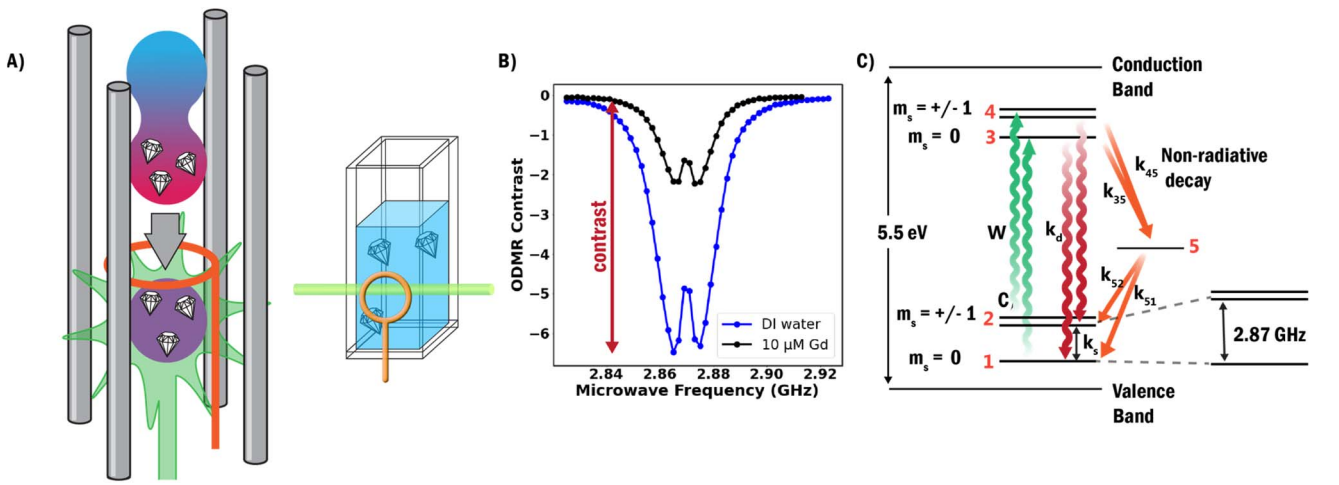


Fig. 1 (A) Microdroplet reaction vessel and cuvette used to measure the ODMR response to $Gd^{+3}$. Two droplets are collided in a quadrupole trap, one with $Gd^{+3}$ and one with NDs, and the resulting droplet is illuminated from below by a 532 nm laser. A circular microwave antenna is inserted into the trap to provide the necessary microwave irradiation for ODMR measurements. (B) Experimental ODMR spectra from a $NV^-$ showing a decrease in fluorescence at the microwave frequencies corresponding to the $m_s = 0$ to $m_s = 1$ and $m_s = -1$ transitions. The splitting between the $m_s = 1$ and $m_s = -1$ levels is due to crystal strain in the nanodiamond. The ODMR response is computed from the ODMR contrast (red arrow) with (black data points) and without (blue data points) $Gd^{+3}$. Lines connecting the data points are provided to guide the eye. (C) The energy level diagram for a $NV^-$ center used in the photophysical model described in Section 2.3.

diameter likely corresponds only to the major axis, with the particle height averaging about a third of the reported diameter as previously discussed.[33] As described below, assumptions about the shape of the ND have large impact on the predicted ODMR response. Estimates of nanodiamond concentration are shown in Table S1.[34] Over the course of an experiment diamonds settle to the droplet dispenser tip, so we estimate from the total fluorescence intensity that the actual concentration could be between 1–30 times larger. The lock-in signal is normalized to the total signal intensity to account for differences in diamond concentration between measurements.

To measure the ODMR spectra (illustrated in Fig. 1B), a microwave antenna is placed inside of the quadrupole trap (Fig. 1A). A signal generator (Stanford Research Systems Inc., Model 384) produces frequencies from 2.825 to 2.925 GHz and is modulated at 1 kHz for lock-in detection. The benefits of lock-in detection for ODMR measurements in a similar system of microfluidic droplets have been previously reported.[35] A microwave amplifier (RF-Lambda #RFLUPA05M03 GB) is connected to a high-power circulator (Fairview Microwave, FMCR1030), which is connected to the microwave antenna. A power meter (Comm-connect) is used to measure the transmitted and reflected microwave power, which averages at ~6 W and 0.1 W, respectively. A laser (Opto Engine, 532 nm, 0.5 W, spot size ~1 $mm^2$) is introduced through the bottom of the trap to excite the $NV^-$ in the NDs, whose fluorescence is measured by a photomultiplier tube (ThorLabs, PMTSS) equipped with appropriate filters (>650 nm). A current preamplifier (Stanford Research Systems Model SR570) records the total fluorescence intensity, which is sent to a lock-in amplifier (Stanford Research Systems SR530) to measure the ODMR signal.

Measurements are performed by colliding two oppositely charged droplets as previously described,[27,29] and measuring the change in ODMR contrast. The ODMR contrast, shown in Fig. 1B, is the difference between the signal off and on the resonance at 2.865 GHz. A droplet with only nanodiamonds collides with a droplet containing a known concentration of $GdCl_3$ (Sigma-Aldrich MKCR6638). As a strongly paramagnetic species with seven unpaired electrons, $Gd^{+3}$ decreases the spin relaxation time ($T_1$) of the $NV^-$ center leading to a decrease in the observed ODMR contrast as shown in Fig. 1B. Here we report the % change in ODMR response to $Gd^{+3}$, which is computed in a self-referential manner from the difference in ODMR contrast with and without gadolinium,

$$\text{ODMR response}(\%) = 100 \times \left(\frac{\text{ODMR contrast}_{\text{no\_Gd}^{+3}} - \text{ODMR contrast}_{\text{Gd}^{+3}}}{\text{ODMR contrast}_{\text{no\_Gd}^{+3}}}\right) \quad (1)$$

Each data point reflects the average of a minimum of three droplet collisions, with error bars indicating one standard deviation.

### 2.2 Bulk measurements

All bulk measurements are performed in a standard cuvette with 45% v/v glycerol as the solvent, which is the same solvent composition used in the droplet measurements described above. A microwave antenna is attached to the side of the cuvette (Fig. 1A). An unfocused 532 nm laser (0.2 W, ~1 $mm^2$ spot size) is directed perpendicular to the PMT to measure the nanodiamond fluorescence. For competitive binding experiments, zinc acetate (Sigma-Aldrich Lot BCBL0315V) and zinc chloride (Sigma-Aldrich Lot MKCP9816) are added to a 1 mM $Gd^{+3}$ aqueous solution of 140 nm diamonds.

### 2.3 Theoretical framework

We develop a photophysical model to explain the experimental data by relating the surface density of $Gd^{+3}$ ($\sigma$) to the measured ODMR response (eqn (1)). In Section 3, we show how analysis of experimental data using Langmuir adsorption models can be used to constrain $\sigma$, which is observed to be a function of $[Gd^{+3}]$, pH, compartment size (*i.e.*, bulk cuvette *vs.* microdroplet) and spectator ions. While these Langmuir models account for the solution phase factors that control $\sigma$, a photophysical model is required to relate the amount of surface adsorbed $Gd^{+3}$ to the actual optical response observed in the experiment. The photophysical model framework described below draws on elements reported in previous studies by Singam *et al.*,[36] Iyer *et al.*,[26] and Tetienne *et al.*[37] while implementing unique descriptions of $\sigma$ and diamond shape in order to comprehensibly capture experimental data. A block diagram describing the organization of the model (Fig. S1), and a glossary of model parameters (Table S2) are included in the SI.

An energy level diagram for a $NV^-$ center is shown in Fig. 1C. In the absence of a magnetic field, the lowest energy state $(1, m_s = 0)$ is separated by 2.87 GHz from the second lowest level $(2, m_s = \pm 1)$. In nanodiamonds, crystal strain lifts the degeneracy of level 2 leading to a pair of transitions at 2.865 GHz and 2.875 GHz as shown in Fig. 1B. Optical excitation ($W$, at 532 nm) from levels 1 → 3 and 2 → 4 is assumed to occur at the same rate and is proportional to laser power. $W$ is a fit parameter in the model, where $W = 1 \times 10^3$ $s^{-1}$ and $2.5 \times 10^3$ $s^{-1}$ is used for the bulk and droplet measurements, respectively. This corresponds to a conversion factor between laser flux and excitation rate of $5 \times 10^3$ $s^{-1}$ $mm^2$ $W^{-1}$.

After excitation, the $NV^-$ decays from levels 4 → 2 and 3 → 1 producing red fluorescence (630–800 nm). The rate constant for these transitions is $k_d = (66 \pm 5) \times 10^6$ $s^{-1}$ as reported in Singam *et al.*[36] Nonradiative decay *via* intersystem crossing to level 5 reduces the fluorescence intensity and occurs more frequently from level 4 than level 3 (*i.e.*, $k_{45} > k_{35}$). Thus, microwave excitation from 1 → 2 at a frequency of 2.865 GHz will reduce the total fluorescence intensity of the nanodiamond as illustrated in Fig. 1B.

The total fluorescence intensity ($I$) is the sum of all the $NV^-$ ($i$) centers in the diamond and depends upon the populations ($N$) of states 1 and 2,

$$I \propto \sum_i (1 - b_1)N_1 + 2(1 - b_2)N_2 \quad (2)$$

where,

$$b_1 = \frac{k_{35}}{k_{35} + k_d} \quad (3)$$

$$b_2 = \frac{k_{45}}{k_{45} + k_d} \quad (4)$$

$k_{35}$, $k_{45}$, $k_{51}$ and $k_{51}$ are rate coefficients governing the transitions between the energy levels illustrated in Fig. 1C and described above. Values for these rate constants are from Singam *et al.*[36] and are shown in Table S3. Singam *et al.*,[36] showed that the following set of rate equations describe the relevant populations *vs.* time needed to compute $I$ in eqn (2),

$$\frac{N_1}{dt} = 2k_s(N_2 - N_1) - Wb_1N_1 + k_{51}N_5 \quad (5)$$

$$\frac{dN_2}{dt} = k_s(N_1 - N_2) - Wb_2N_2 + k_{52}N_5 \quad (6)$$

$$\frac{dN_5}{dt} = W(b_1N_1 + 2b_2N_2) - (k_{51} + 2k_{52})N_5 \quad (7)$$

where $N_1$, $N_2$, and $N_5$ are the populations of energy levels 1, 2, and 5, respectively. The steady state populations of $N_1$ and $N_2$, obtained by numerically solving eqn (5)–(7), are used to compute the expected fluorescence intensity ($I$) in eqn (2).

The fluorescence intensity ($I$, in eqn (2)) depends upon [$Gd^{+3}$] *via* $k_s$ in eqn (5) and (6), which governs the transition rate between levels 1 and 2. In the presence of resonant microwave excitation, $k_s$, is a function of the spin relaxation time ($T_1$) of the $NV^-$ center,

$$k_s = \frac{1}{3T_1} + \frac{2 \times \Omega/T_m}{(2\Omega)^2 + (1/T_m)^2}\Omega \quad (8)$$

where $\Omega$ is the Rabi frequency between states 1 and 2. We estimate[36] $\Omega$ to be $9 \times 10^6$ rad $s^{-1}$, with some uncertainty due to microwave inhomogeneity. However, as we describe below, the model itself is only weakly dependent on $\Omega$. $T_m$ encompasses all of the processes responsible for dephasing,

$$T_m = \frac{1}{\frac{1}{T_2} + W} \quad (9)$$

where we estimate the $T_2$ value from ref. 38 to be $1.5 \times 10^{-7}$ $s^{-1}$. $T_1$ depends on the $NV^-$ location within the nanodiamond and its proximity to $Gd^{+3}$ and is,

$$\frac{1}{T_1} = \frac{1}{T_{1,Bulk}} + 3\gamma_e{}^2 B_\perp{}^2 \frac{\tau_c}{1 + f^2\tau_c{}^2} \quad (10)$$

where $f = 2\pi \times 2.865$ GHz, and $B_\perp{}^2$ is the variance in the transverse magnetic field in the presence of surface adsorbed $Gd^{+3}$. $T_{1,Bulk}$ is assigned a value of 2 ms following ref. 37. From Tetienne *et al.*,[37] the correlation time of the magnetic field ($\tau_c$) in eqn (10) is,

$$\frac{1}{\tau_c} = \frac{\mu_0\gamma_e{}^2\hbar\sqrt{6}C_s}{4\pi}\sqrt{\frac{\pi}{2}}\frac{\sigma^{0.5}}{r_{min}{}^2} + R_{vib} \quad (11)$$

where (see Table S4) $\mu_0$ is the vacuum permeability, $\gamma_e$ is the electron gyromagnetic ratio, $\sigma$ is the surface spin density, and $r_{min} = 0.15$ nm, which is the nearest neighbor distance in the diamond lattice.[37] $R_{vib}$ is the contribution from intrinsic vibrational spin relaxation and is assigned a value of 1 $ns^{-1}$.[26,37] At concentrations below 1 mM, free $Gd^{+3}$ ions in solution should have a negligible effect on the $NV^-$ center, so we consider only the contribution of ions adsorbed to the surface of the ND.[26] $B_\perp{}^2$ can be computed by summing over the contributions from each of the surface spins, $i$,[26,36]

$$B_\perp{}^2 = \sum_i B_{\perp,i}{}^2 = \left(\frac{\mu_0\gamma_e\hbar}{4\pi}\right)^2 2\pi C_s\sigma\frac{4}{R^6} \quad (12)$$

where $C_s$ is a coefficient related to the spin quantum number. For $Gd^{+3}$ with its 7/2 spin state, $C_s = \frac{21}{4}$. The value of $C_s$ is specific to the ion being modeled and must be recalculated for different ions such as $Fe^{+3}$ or $Cu^{+2}$, using $C_s = S(S+1)/3$, where $S$ is the spin quantum number. $R$ is the distance of a surface spin to an $NV^-$ in the ND as shown in Fig. 2A. $\sigma$ can be related to the aqueous [$Gd^{+3}$] by a Langmuir isotherm,

$$\sigma = \Gamma_\infty(\mathrm{pH}) \cdot \theta \quad (13)$$

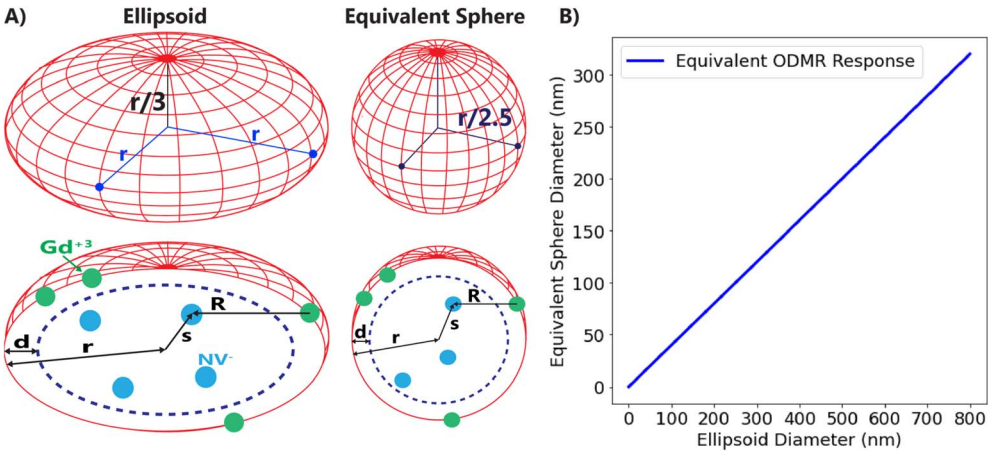


Fig. 2 (A) Ellipsoid and equivalent sphere models of ND with a hydrodynamic radius of r. Blue circles represent $NV^-$ and green circles correspond to adsorbed $Gd^{+3}$. $R$ is the distance between a $NV^-$ positioned at s to the surface. $d$ is the exclusion distance of $NV^-$ from the surface. (B) The ellipsoid shape with an aspect ratio of 3 yields an equivalent ODMR response as a smaller sphere with a radius of $r$/2.5.

where the fractional surface coverage ($\theta$) is,

$$\theta = \left(\frac{K_{\text{eq.}}\left[\text{Gd}^{+3}\right]}{1 + K_{\text{eq.}}\left[\text{Gd}^{+3}\right]}\right) \tag{14}$$

The Langmuir model is one of the simplest adsorption isotherms that connect the surface coverage with the bulk concentration of an adsorbate. The model restricts adsorbates to monolayer coverage (*i.e.*, $\theta = 1$) and assumes a set of uniform non-interacting surface adsorption sites. $\Gamma_\infty$ is the maximum site concentration, which as will be shown below, is a function of pH ($\Gamma_\infty$(pH)). We assume that $Gd^{+3}$ occupies a single site. $\theta$ depends upon $K_{\text{eq}}$ (units of $M^{-1}$); the equilibrium constant governing the partitioning of solution phase $Gd^{+3}$ to the ND surface.

If the ND is assumed to be a sphere, Iyer *et al.*[26] showed that eqn (12) is,

$$B_\perp{}^2 = \left(\frac{\mu_0\gamma_e\hbar}{4\pi}\right)^2 2\pi C_s\sigma\frac{r}{s}\left(\frac{1}{(r-s)^4} - \frac{1}{(r+s)^4}\right) \tag{15}$$

where $s$ is the location of the $NV^-$ within a sphere of radius, $r$, as shown in Fig. 2A. However, approximating the ND as a sphere using its hydrodynamic diameter, as we show below, leads to substantial inaccuracies in predicting the ODMR response observed in our experiments. This is because the interaction of a spin with the $NV^-$ is short range (nanometers) so the assumed ND shape governs the average distance $R$ of an $NV^-$ to the surface of the diamond where the adsorbed $Gd^{+3}$ resides.

Indeed, nanodiamonds, in the size range used here, are non-spherical and have irregular disk or rod-like shapes, which substantially alter the average $NV^-$-to-surface distance relative to that of a sphere.[33,39,40] Eldemrdash *et al.*[33] report an average length-to-height aspect ratio of 3.8 for 140 nm diamonds, and an average ratio of 3 for all diamond sizes they examined. So, the average height of the 140 nm ND is on the order of 36 nm. This suggests that a 140 nm disk-shaped diamond should have an effective sensitivity equivalent to a much smaller spherically shaped particle. As a more realistic approximation for the actual ND shape, we use an ellipsoid to compute $R$ in eqn (12) using the law of cosines. The ellipsoid, illustrated in Fig. 2, has the following dimensions in spherical coordinates,

$$x = \frac{r}{3}\cdot\cos\theta \tag{16}$$

$$y = r\cdot\sin\theta\cdot\cos\varphi \tag{17}$$

$$z = r\cdot\sin\theta\cdot\sin\varphi \tag{18}$$

where $z$ in the height of the ellipsoid and $r$ is the hydrodynamic radius. Using an ellipsoid shape to solve for $R$ in eqn (12) yields the following expression for $B_\perp{}^2$:

$$B_\perp{}^2 = \left(\frac{\mu_0\gamma_e\hbar}{4\pi}\right)^2 4C_s\sigma\int_0^{2\pi}\int_0^{\pi}\frac{\sqrt{r^4(5+4\cos 2\theta)}\sin\theta}{3\left(\left(s\cos\theta_s - \frac{1}{3}r\cos\theta\right)^2 + (r\cos\varphi\sin\theta - s\cos\varphi_s\sin\theta_s)^2 + (r\sin\varphi\sin\theta - s\sin\varphi_s\sin\theta_s)^2\right)^3}\mathrm{d}\theta\mathrm{d}\varphi \tag{19}$$

where ($s$, $\theta_s$, $\varphi_s$) are the coordinates of the $NV^-$ center. Eqn (19) is solved numerically in *Mathematica*.[41] The total fluorescence intensity is then computed by averaging the $I$ values calculated on an evenly spaced grid within the ellipsoid.

Numerically solving eqn (19) is time-consuming, so instead we use an equivalent sphere approximation to the ellipsoid geometry shown in Fig. 2A. As shown in Fig. 2B the ODMR response computed for the full ellipsoid model equates to the response computed for a sphere with an effective radius that is approximately 2.5 times smaller than the maximum elliptical radius, $r$ (Fig. 2A). This scaling is consistent with previous calculations from Eldemrdash *et al.*[33] The equivalent sphere approximation is used to model all experimental data presented below unless otherwise stated. In both the equivalent sphere and ellipsoid models, it is assumed that there are no $NV^-$ centers within 6 nm of the diamond surface (d, Fig. 2A), since these shallow $NV^-$ centers are often in the $NV^0$ state.[26,33] This is in agreement with prior studies, which have found this depth to be between 6–10 nm.[26,33]

## 3. Results and discussion

The photophysical model described above is used to explain the ODMR response observed in experiments described below. To do this, the experimental data is analyzed using a Langmuir adsorption model to link the solution phase concentration of $Gd^{+3}$ to the surface adsorbed population of gadolinium spins ($\sigma$) that are detected by the $NV^-$ center. Integrating Langmuir adsorption isotherms within a photophysical model enables the ODMR response to be predicted as a function of pH, micro scale confinement, and competitive binding with results that are consistent across different experimental set-ups. In the following section, each experimental data point reflects the average of a minimum of three trials, with error bars indicating one standard deviation.

### 3.1 ODMR response *vs.* $[Gd^{+3}]$ and pH in bulk samples

Shown in Fig. 3A is the ODMR response as a function of $[Gd^{+3}]$ and pH (2.5, 4.1, 6.4, and 11). These curves are highly non-linear (note log $x$-axis). For example, at pH = 11 a 1000× change in $[Gd^{+3}]$ (from 0.1 to 10 μM) produces only a ∼5× increase in ODMR response (∼15 to 70%). In addition to $[Gd^{+3}]$, the ODMR

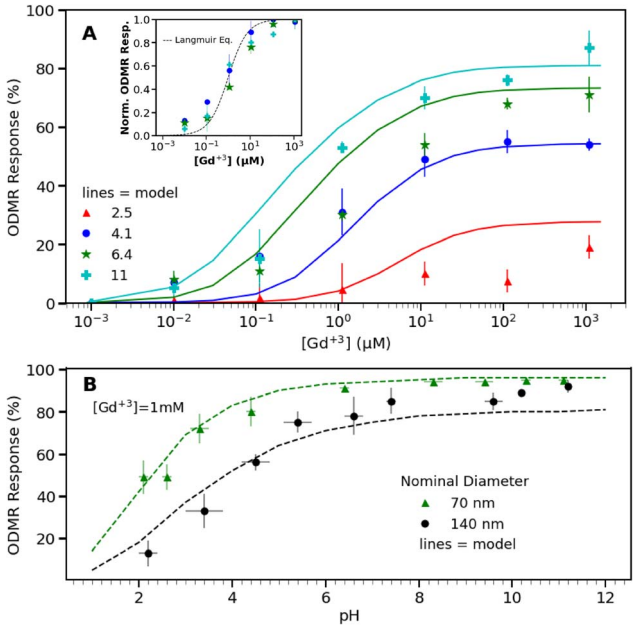


Fig. 3 (A) ODMR response at 2.865 GHz *vs.* $[Gd^{+3}]$ and pH (2.5, 4.1, 6.4 and 11). These measurements used 140 nm diamonds in bulk solution. Symbols represent experimental data. The ODMR response is modeled (solid lines: equivalent sphere model) using the photophysical model with surface spin density modeled by a Langmuir adsorption isotherm (eqn (13)) with an equilibrium constant of $1 \times 10^5$ $M^{-1}$ (eqn (14)). (Inset) Normalized ODMR response *vs.* $[Gd^{+3}]$ with a function representing the Langmuir isotherm (dashed line). (B) ODMR response at $[Gd^{+3}] = 1$ mM *vs.* pH for 70 and 140 nm nanodiamonds (symbols represent experimental data). Dashed lines are results from photophysical model using the equivalent sphere approximation. Nominal diameter refers to the hydrodynamic diameter obtained in dynamic light scattering experiments.

response in Fig. 3A is observed to be a strong function of pH. At pH = 11 the ODMR response saturates at ~80% for $[Gd^{+3}] > 100$ μM, whereas this plateau decreases to 10–15% for pH = 2.5 at $[Gd^{+3}] > 100$ μM. Despite the differences in where the ODMR response saturates with pH, the overall shapes of the curves are nearly identical as illustrated in the inset of Fig. 3A, where the curves are normalized to the maximum ODMR response at $[Gd^{+3}] = 1$ mM. Also included in the inset for a qualitative comparison is the functional form of the Langmuir equation (eqn (13)) showing that the non-linear behavior is consistent with a sensing modality that requires physical adsorption of the gadolinium to the ND surface. The non-linearity of the curves in Fig. 3A is important when considering the sensitivity of nanodiamonds for measuring paramagnetic species. For instance, the optimal sensing range is governed by the location of the inflection point in the curve where ODMR response is most sensitive to changes in $[Gd^{+3}]$.

The pH dependence of the ODMR response at $[Gd^{+3}] = 1$ mM is shown explicitly in Fig. 3B. In addition to pH, the ODMR response is also observed to be a function of ND size (70 nm *vs.* 140 nm), which will be discussed in more detail below. At pH = 10 the ODMR response is large and plateaus at 92% and 95% for the 140 and 70 nm diamonds, respectively. There is little sensitivity below pH 2.2 for the 140 nm diamonds with an ODMR response of 13% for $[Gd^{+3}] = 1$ mM. The strong pH dependence of these curves, also noted in previous studies, introduces the possibility of this system as a simple pH probe.[42,43]

The shape of the 140 nm pH curve in Fig. 3B closely resembles the measured zeta potential for carboxylated nanodiamonds shown in Fig. S3. Although the zeta potential depends on a number of factors such as ionic strength, the shape of the curve is often used to estimate the $pK_a$ of surface functional groups.[44,45] Prior literature identified a $pK_a$ of 4 and 4.5 for carboxyl and hydroxyl groups on the nanodiamond surface.[42,46] The inflection point of the ODMR response for the 140 nm diamonds coincides with this $pK_a$ range (4.4), whereas the inflection point in the ODMR response for the 70 nm ND is shifted to smaller pH values. This difference between the 140 and 70 nm ND is likely due to a saturation in the ODMR response for the 70 nm diamonds at high pH (>6) distorting the shape of the curve.

The characteristic shape of ODMR response *vs.* pH (Fig. 3B) and its correspondence with the zeta potential implies that $Gd^{+3}$ sensing depends upon the charge state of the functional groups on the nanodiamond surface. At lower pH the negatively charged carboxylate groups ($-COO^-$) protonate (–COOH); no longer efficiently electrostatically binding $Gd^{+3}$ and inhibiting efficient sensing. Thus, the pH dependence observed in Fig. 3B is assumed to reflect the change in maximum concentration of carboxylate binding sites, $\Gamma_\infty$ (pH). Since the ODMR response and zeta potential both asymptote at pH = 10–12, it is reasonable to conclude that this is the region where the surface is fully deprotonated with a maximum site concentration of $\Gamma_\infty^{max} = 8.5 \times 10^{17}$ $m^{-2}$, which is in agreement with Panich *et al.*[47] and the range determined by Tetienne *et al.*[37] and Iyer *et al.*[26] who report $\Gamma_\infty^{max} = 4 \times 10^{18}$ $m^{-2}$ and $6 \times 10^{17}$ $m^{-2}$, respectively.[37,48] The pH dependence of $\Gamma_\infty$ (pH) in Fig. 3B is parameterized using a logistic function,

$$\Gamma_\infty(\mathrm{pH}) = \frac{\Gamma_\infty^{max}}{(1+e^{-0.62\cdot(\mathrm{pH}-5.4)})^{1.5}} = \frac{8.5\times10^{17}}{(1+e^{-0.62\cdot(\mathrm{pH}-5.4)})^{1.5}} \quad (20)$$

which is used in eqn (13) to predict ODMR response.

Results of the photophysical model are plotted in Fig. 3A and B. These model results (Fig. 3A and B) use the equivalent sphere approximation, which produces nearly identical results to the full ellipsoid geometry as shown in Fig. S2. The ODMR response as a function of both pH and $[Gd^{+3}]$ is replicated using $K_{eq} = (1 \pm 0.5) \times 10^5$ $M^{-1}$ in eqn (14). The model replicates the trends in the data using a single value for $K_{eq}$, which suggests that the ODMR response at these concentrations is mainly sensitive to adsorbed $Gd^{+3}$ and not to free $Gd^{+3}$ in solution. This also confirms that changes in pH mainly control the availability of surface sites ($\Gamma_\infty$) rather than the thermodynamics of $Gd^{+3}$ binding to the surface (*i.e.*, $K_{eq}$) as suggested by the similar shape and inflection point of the normalized curves shown regardless of pH (see inset of Fig. 3A). This observation is consistent with previous studies of the adsorption of $Gd^{+3}$ or other metal cations to the carboxyl and hydroxyl functionalized nanodiamonds.[24,25]

Assuming an activity coefficient ($\alpha_c$) of 1 and a standard reference solution concentration of 1 M, $K_{eq}$ is related to the free energy of adsorption ($\Delta G°$) by,[49,50]

$$\Delta G° = -RT \cdot \ln\left(\frac{K_{eq}}{\alpha_c} \cdot 1\ \mathrm{M}\right) \quad (21)$$

where $T$ is the temperature (293.15 K) and $R$ is the gas constant. $\Delta G°$ is computed to be $(-28 \pm 1)$ kJ mol$^{-1}$. The large negative value of $\Delta G°$ shows that the adsorption of $Gd^{+3}$ to the carboxylated nanodiamond surface is quite thermodynamically favorable and spontaneous. This value is similar in magnitude to the $\Delta G°$, recomputed using eqn (21), determined for the adsorption of cationic malachite green dye to the surface of negatively charged polystyrene beads ($(-56.2 \pm 0.4)$ kJ mol$^{-1}$, ($(-55.3 \pm 8)$ kJ mol$^{-1}$)).[50,51]

It is important to note that the value of $K_{eq}$ determined using the full photophysical model is not equivalent to that obtained by a fit to the normalized curves shown in the inset of Fig. 3A. This implies that the ODMR response is not solely determined by $\theta$, since changes in laser and microwave power and ND size can shift the inflection point of the curve even when $K_{eq}$ is held constant.

To illustrate this further and to check the broader applicability of our model, we compare our measurements and model results with those reported by Sarkar *et al.*[35] As shown in Fig. 4, over a similar range of $[Gd^{+3}]$, Sarkar *et al.*[35] measured a much smaller ODMR response than is observed here. At $[Gd^{+3}] = 10$ μM, Sarkar *et al.*[35] observed an ODMR response of 16%, whereas for the same concentration at a similar pH, we observe a response of 54% (Fig. 4). This difference is explained by the larger laser flux (~10–40 Watts per mm$^2$), microwave power (21 W, $\Omega = 1.1 \times 10^7$ rad s$^{-1}$) and smaller ND size (hydrodynamic diameter = 40 nm, corresponding to an equivalent sphere radius of 8 nm) used by Sarkar *et al.*[35] Accounting for these differences and using the value of $K_{eq}$ determined here, the smaller ODMR response is replicated by our model as shown in Fig. 4. This agreement between model and their observations is obtained using $W = 1 \times 10^6$ s$^{-1}$, which is approximately 5 times larger than the value predicted using the proportionality constant of $5 \times 10^3$ s$^{-1}$ mm$^2$ W$^{-1}$ described above, which likely arises from uncertainties in laser flux due to spot size or other effects arising from the smaller diamond size. Although Sarkar *et al.*[35] used water as the solvent, rather than the water/glycerol mixture used here, we found that the ODMR response is insensitive to these solvent differences as shown in Fig. S4.

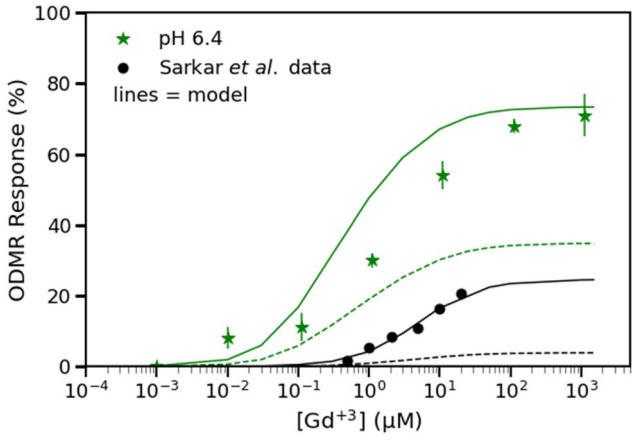


Fig. 4 Measured (points) and modeled (lines) ODMR response *vs.* $[Gd^{+3}]$. The data at pH = 6.4 is measured using ND with a hydrodynamic diameter of 140 nm (green stars). The data reported by Sarkar *et al.*[35] (black circles) use ND with an average hydrodynamic diameter of 40 nm. Solid lines are from the photophysical model using the equivalent sphere approximation to the ellipsoid. The dashed lines are model predictions using a sphere whose dimensions correspond to the hydrodynamic diameters of the ND.

### 3.2 Effects of nanodiamond shape

As discussed above, the spherical approximation to an ellipsoid (solid lines, Fig. 4) provides a reasonable accounting of the 140 nm data observed here as well as reported by Sarkar *et al.*[35] using a smaller ND (40 nm). Alternatively, as shown using dashed lines in Fig. 4, the ODMR response is substantially underpredicted if we assume instead spheres whose dimensions correspond to hydrodynamic diameters of 140 nm and 40 nm. For the pH = 6.4 data set in Fig. 4, the ODMR response at $[Gd^{+3}] = 10$ μM, assuming a hydrodynamic diameter, is ~2× smaller than the observations and model whereas in the case of Sarkar *et al.*, at $[Gd^{+3}] = 10$ μM the ODMR is underpredicted by ~6×. These comparisons illustrate the importance of ND shape since the assumed nanodiamond shape controls the average distance the $NV^-$ is to the surface, which in turn controls the strength of the interaction between the color center with the surface adsorbed $Gd^{+3}$ spins.

### 3.3 Competitive binding of $Gd^{+3}$

In any complex aqueous or biological environment there are likely to be a complex array of molecules (*e.g.* ligands or other reactive species) and ions (*e.g.*, buffers) that can directly or indirectly influence the ODMR response to parametric analytes. For example, background ions can directly compete with $Gd^{+3}$ for binding to nanodiamond surface as illustrated above where the pH dependence is shown to arise from competitive adsorption/neutralization of surface carboxylate groups by $H^+$, thus preventing $Gd^{+3}$ binding. Alternatively, molecules in solution (*e.g.*, ligands) complex with $Gd^{+3}$ preventing efficient adsorption to the ND surface and subsequent detection. We examine this by adding zinc chloride and zinc acetate to a 1 mM gadolinium solution containing 140 nm ND. As shown in Fig. 5, the addition of zinc chloride does not alter the ODMR response indicating that $Zn^{+2}$, at these concentrations, does not directly compete with $Gd^{+3}$ for surface binding sites. At much higher concentrations (>250 mM) this may not be the case, as illustrated by Iyer *et al.*[26] for competitive surface binding of $Na^+$ and $Gd^{+3}$. Competitive adsorption in a Langmuir framework has been explored previously,[52] and an equation for $\theta$ to account for competitive surface binding is included in the SI (eqn S1)."

The introduction of zinc acetate (Fig. 5), however, produces a marked decrease in ODMR response over the same

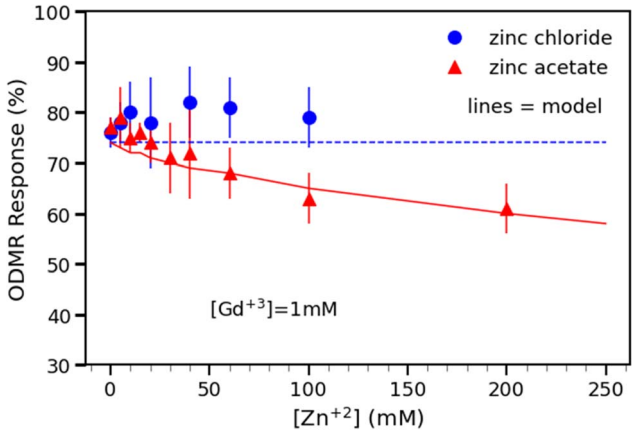


Fig. 5 ODMR response at $[Gd^{+3}] = 1$ mM as a function of $[ZnCl_2]$ and [Zn-acetate]. This data was collected using 140 nm diamonds at pH 6.6 in bulk solution. For Zn-acetate, the photophysical model uses the surface spin density computed by the competitive binding model (red solid line, eqn (25)). The blue dashed line corresponding to $ZnCl_2$ is the standard photophysical model that utilizes eqn (14).

concentration range, suggesting less binding of $Gd^{+3}$ to the nanodiamond surface. Since the $ZnCl_2$ data clearly shows that $Zn^{+2}$ does not compete with $Gd^{+3}$ for surface sites, we conclude that it is the formation of $Gd^{+3}$ acetate complexes in solution that reduce the ODMR response. This is likely because $Gd^{+3}$ that is complexed with the negatively charged acetate ligand does not efficiently bind to the ND surface. To explain these observations quantitatively, the competition between acetate ligand complexation and ND surface adsorption is incorporated into a modified Langmuir adsorption model. The adsorption equilibrium of $Gd^{+3}$ to a ND surface site to form an adsorbed species ($Gd_{ads}{}^{+3}$) is,

$$\text{site} + Gd^{+3} \leftrightharpoons Gd_{ads}{}^{+3} \quad \text{(R1)}$$

where sites is a volumetric concentration. The volumetric concentration of sites ([site]), rather than simply the average surface density, is required since the competition for $Gd^{+3}$ is not at the ND surface but rather with a species in solution. [site] is estimated using the average diamond concentration in the sample, the total surface area and the surface density of carboxylate groups as shown in Table S1. The estimated value for [site] is 1 μM.

$Gd^{+3}$ adsorption to the ND surface competes with its complexation with free acetate (A) in solution,

$$A + Gd^{+3} \leftrightharpoons GdA \quad \text{(R2)}$$

where GdA is the ligand complex. For simplicity, the exact speciation of $Gd^{+3}$ ligand complexes with acetate (*i.e.*, $Gd^{+3}$-$(acetate)_2$ and $Gd^{+3}$-$(acetate)_3$) is neglected in the model since there is no way to determine the individual binding equilibria of each of these species to the nanodiamond surface. Thus, we assume that GdA represents all possible complexes of $Gd^{+3}$ with acetate, which are assumed not to bind to the nanodiamond surface.

The equilibrium constants, $K_{eq}$ and $K_{eq,2}$, for adsorption in R1 and ligand complexation in R2 are,

$$K_{eq} = \frac{[Gd_{ads}{}^{+3}]}{[Gd^{+3}]([site] - [Gd_{ads}{}^{+3}])} \quad (22)$$

$$K_{eq,2} = \frac{[GdA]}{[Gd^{+3}]\cdot[A]} \quad (23)$$

The total $[Gd^{+3}]_0$ in the system is,

$$[Gd^{+3}]_0 = [Gd^{+3}] + [Gd_{ads}{}^{+3}] + [GdA]. \quad (24)$$

where $[Gd^{+3}]_0$ is known from the initial solution concentration. Solving for $\theta = \frac{[Gd_{ads}{}^{+3}]}{[site]}$, in *Mathematica*,[41] using $K_{eq}$, $K_{eq,2}$ and eqn (24) yields,

$$\theta = \frac{1 + [Gd^{+3}]_0 K_{eq} + [A]K_{eq,2} + [site]K_{eq} - \sqrt{4[Gd^{+3}]_0(K_{eq} + [A]K_{eq,2}K_{eq}) + \left(1 - [Gd^{+3}]_0 K_{eq} + [A]K_{eq,2} + K_{eq}[site]\right)^2}}{2K_{eq}[site]} \quad (25)$$

Using the Visual MINTEQ software,[53] $K_{eq,2}$ is estimated to be 800 $M^{-1}$.[53] Assuming that only free $Gd^{+3}$ can bind to the nanodiamond surface, $\sigma$ is computed using eqn (25). The photophysical model predicting ODMR response *vs.* [Zn-acetate] shows reasonable agreement with the experimental results in Fig. 5. $Gd^{+3}$ has a much stronger affinity for the nanodiamond surface than for the acetate ligand ($K_{eq} = \sim 125 \times K_{eq,2}$) and explains why it requires 0.25 M of acetate to induce an appreciable change in the ODMR response. The predicted shift in the ODMR response *vs.* $[Gd^{+3}]$ and as a function of [Zn-acetate] is shown in Fig. S5. For an ODMR response of 50%, the presence of 0.02 M Zn-acetate shifts the expected total $Gd^{+3}$ concentration by a factor of about 100 (SI, Fig. S5). The trend shown in Fig. 5 would be expected to vary in complex ways since both the acetate speciation with $Gd^{+3}$ and the number of carboxylate surface binding sites are pH dependent.

The results presented above illustrate how pH, assumptions about ND shape, and charged ligands in solution alter the ODMR response to paramagnetic species in solution. The presence of background ions in solutions can either directly or indirectly influence the adsorption of $Gd^{+3}$ to the ND surface. Increasing $[H^+]$ reduces the fraction of carboxylate adsorption sites for $Gd^{+3}$ thus reducing the ODMR response. Alternatively,

charged ligands (acetate) in solution alter the response by sequestering free $Gd^{+3}$ and preventing its adsorption to the ND surface. The magnitude of this competition depends upon both the difference in equilibrium constants ($K_{eq}$ *vs.* $K_{eq,2}$) and the absolute concentration of carboxylate binding sites *vs.* [acetate]. These two effects are quantitatively explained within a self-consistent Langmuir framework and by assuming that the ND are non-spherical and approximately ellipsoidal. These measurements, conducted in macroscale bulk samples (cuvette), provide a baseline for examining additional factors such as ND and compartment size using microdroplets described below.

### 3.4 ODMR response *vs.* ND size in microdroplets

ND are often envisioned as novel probes of paramagnetic species (free radicals, metals, *etc.*) in microenvironments such as cells. Thus, it is important to understand how both the size of ND and the microenvironment itself alters the ODMR response. To do this, we measure the ODMR response *vs.* $[Gd^{+3}]$ and ND size in microdroplets (radius = 17 μm) as shown in Fig. 6A. At a given $[Gd^{+3}]$ the smaller ND produce a much larger ODMR response. For example, at $[Gd^{+3}]$ = 1 mM the 70 nm nominal diameter particle exhibits a response (*i.e.* 70%) that is 2× and 10× larger than the 140 nm and 750 nm ND, respectively. Furthermore, as observed for the pH dependent studies described above and shown in Fig. 6A, the value at which the ODMR response saturates (*i.e.*, $[Gd^{+3}]$ > 100 μM) is size dependent.

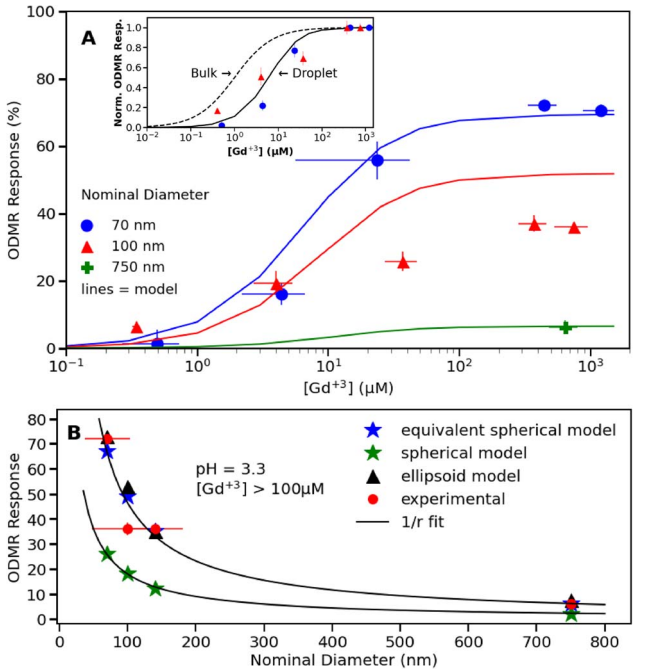


Fig. 6 (A) ODMR response *vs.* $[Gd^{+3}]$ and ND size (70, 100, 750 nm) at a pH = 3.3. Experimental data is represented by symbols. The photophysical model prediction is shown as lines using eqn (27) to compute the spin surface density ($\sigma$). (inset) Normalized ODMR response *vs.* $[Gd^{+3}]$ and ND size (70, 100, 750 nm). For comparison the normalized ODMR response for bulk solutions is shown as a dashed line. (B) ODMR response *vs.* ND size for $Gd^{3+}$ > 100 μM at pH = 3.3 (red circles). These measurements were performed in droplets. Black solid line shows a 1/*r* functional form. Photophysical model predictions for the four diamond sizes (70, 100, 140, 750 nm) are shown assuming both an equivalent sphere (blue stars) and ellipsoid (black triangles) for the ND shape. Green stars correspond to model predictions assuming a sphere whose dimensions are computed from the hydrodynamic diameter.

The normalized ODMR response *vs.* $[Gd^{+3}]$ is shown in the inset of Fig. 6A. For each particle size, these curves are normalized by the maximum ODMR response observed at saturation (*i.e.*, $[Gd^{+3}]$ > 100 μM). The normalized size dependence collapses onto a common curve whose shape resembles that of a Langmuir isotherm (inset Fig. 6A). This comparison shows the overall shape of the ODMR *vs.* $[Gd^{+3}]$ is independent of ND size and that the key difference observed in Fig. 6 is the level at which the ODMR response saturates. This similarity in shape for different sized ND suggests that the thermodynamics of $Gd^{+3}$ adsorption (*i.e.*, $K_{eq}$) does not depend upon size. However, as shown in the inset of Fig. 6A, there is a substantial difference between the normalized ODMR response *vs.* $[Gd^{+3}]$ for bulk cuvette and droplet measurements. This difference can be clearly seen by noting the concentration where the normalized ODMR response is 0.5. For the bulk measurement this occurs at 1 μM, which is nearly a factor of 10 smaller than for the microdroplet case, which occurs at $[Gd^{+3}]$ ~10 μM.

The shift in $Gd^{+3}$ sensitivity between the cuvette and microdroplet cannot be rationalized by a change in $K_{eq}$, since for bulk measurements a single value of $K_{eq}$ replicated the ND size dependence shown in Fig. 3B. Thus, we conclude that this shift in sensing is due to the microenvironment itself. As discussed previously by Wilson and Prophet,[54] on average only a small fraction of the total number of solute molecules reside at interfaces (*e.g.*, gas–liquid or ND-liquid) in beaker-scale aqueous solutions, which is often not the case for microdroplets where, depending on the concentration and compartment size, a substantial portion of the total molecules in a droplet reside at the interface. This is simply a consequence of the small volume of microdroplets, which require fewer numbers of solute molecules to achieve the same concentration as in a macroscale beaker or cuvette. As will be shown below, the high surface area of the ND relative to the total number of $Gd^{+3}$ in a microdroplet leads to substantial change in bulk $[Gd^{+3}]$ upon adsorption.

The volumetric diamond site concentration in the droplet is on average 10 μM and ~10× larger than in the bulk sample discussed above (see Table S1). This large site concentration can lead to solute depletion within the droplet where free $Gd^{+3}$ is depleted from the solution by its adsorption to the diamond surface; a consequence of the finite droplet volume as discussed previously.[54–56] For this case, the simple Langmuir isotherm (eqn (13)), which explicitly assumes that adsorption does not alter the bulk concentration of the adsorbate, is no longer valid. Allowing the concentration of free $Gd^{+3}$ to decrease as it adsorbs to the surface of the diamond requires a modified equation for $\theta$.

The rate law based upon the Langmuir equation is,

$$\frac{\mathrm{d}\left[\mathrm{Gd_{ads}}^{+3}\right]}{\mathrm{d}t} = k_1\left(\left[\mathrm{Gd}^{+3}\right]_o - \left[\mathrm{Gd_{ads}}^{+3}\right]\right)\left([\mathrm{site}] - \left[\mathrm{Gd_{ads}}^{+3}\right]\right) - k_{-1}\left[\mathrm{Gd_{ads}}^{+3}\right] \quad (26)$$

where $K_{eq} = \frac{k_1}{k_{-1}}$ and $k_1$ and $k_{-1}$ are the rate constants governing adsorption and desorption, respectively. [site] is the total concentration of surface sites, so [site] − $[\mathrm{Gd_{ads}}^{+3}]$ is the concentration of free sites. Likewise, $[\mathrm{Gd}^{+3}]_0$ is the total concentration of $Gd^{+3}$, so $[\mathrm{Gd}^{+3}]_0 - [\mathrm{Gd_{ads}}^{+3}]$ is the concentration of $Gd^{+3}$ in solution only. Finally, $\frac{\mathrm{d}[\,\mathrm{Gd_{ads}}^{+3}]}{\mathrm{d}t}$ is set to zero to compute the steady state $[\mathrm{Gd_{ads}}^{+3}]$. Solving for $\frac{[\mathrm{Gd_{ads}}^{+3}]}{[\mathrm{site}]}$, which is equivalent to $\theta$ yields,

$$\theta = \frac{1 + K_{eq}\left(\left[\mathrm{Gd}^{+3}\right] + [\mathrm{site}]\right) - \sqrt{\left[\mathrm{Gd}^{+3}\right]^2 {K_{eq}}^2 - 2\left[\mathrm{Gd}^{+3}\right]K_{eq}\left(K_{eq}[\mathrm{site}] - 1\right) + \left(1 + K_{eq}[\mathrm{site}]\right)^2}}{2K_{eq}[\mathrm{site}]} \quad (27)$$

The magnitude of $K_{eq}$ should not differ between the droplet and bulk environments since the energetics of adsorption to the nanodiamond surface should be identical. Thus, $K_{eq}$ extracted from the bulk data ($(1 \pm 0.5) \times 10^5\ \mathrm{M}^{-1}$) is used to model the microdroplet data in Fig. 6.

As shown in Fig. 6A, the absolute value of the ODMR response also depends upon ND size. This is further illustrated in Fig. 6B where the ODMR response at $[\mathrm{Gd}^{+3}]$ ~1 mM is a function of nominal ND diameter. The ODMR response at 70 nm is 72% and dramatically decreases to 6% for 750 nm ND. The overall trend follows a $1/r$ dependence, suggesting surface-to-volume scaling. This scaling behavior can be understood conceptually if one assumes that the $NV^-$ centers are evenly distributed through the nanodiamond volume; a reasonable assumption given current fabrication methods.[39] $NV^-$ centers located nearer to the diamond surface exhibit greater sensitivity to $Gd^{3+}$ compared to those near the core due to the $R^{-6}$ scaling of the interaction strength.[57] Consequently, 70 nm diamonds, which have a larger fraction of their overall $NV^-$ centers closer to the surface relative to a 140 nm particle, display a larger observed ODMR response. However, $NV^-$ centers near the surface of the diamond to a depth of <10 nm are likely to be in the $NV^0$ charge state and therefore unable to sense $Gd^{+3}$.[58–60] In our model, we assume that all $NV^-$ centers in a shell that is 6 nm deep on the surface of the diamond are in this state and insensitive to $Gd^{+3}$ as shown in Fig. 2.[48]

The expression for $\theta$ in eqn (27), which explicitly accounts for the solution phase depletion of $Gd^{+3}$ is used to compute $\sigma$ (eqn (13)) in the full photophysical model. The model replicates the ODMR response *vs.* $[\mathrm{Gd}^{+3}]$ and nominal ND diameter observed in microdroplets using a pH of 3.3, which is slightly smaller than the measured solution pH prior to dispensing it to form a droplet (3.9 ± 0.2). This is not entirely unexpected, since droplet pH can vary from bulk pH, is difficult to measure, and in some cases gradients are reported to exist.[1,61]

Relative to the 70 and 750 nm data sets, the model overestimates the ODMR response for the 100 nm diamonds. This may be a result of the larger uncertainty and/or broader size distribution in this size range. This reflects a current limitation of our model, which assumes a single ND size rather than a distribution. Future model improvements will include more realistic representations of the ND size distribution. The normalized photophysical model is shown in Fig. 6A (inset) for both the bulk and droplet samples. Using a single value of $K_{eq}$, the model correctly predicts the rightward shift in the droplet calibration curves by taking $Gd^{+3}$ depletion into account. The model in both cases correctly predicts the absolute magnitude of the ODMR response *vs.* size and pH shown in Fig. 6B and 3B, respectively. It should be pointed out that whereas various assumptions about ND shape (sphere *vs.* ellipsoid) all produce $1/r$ scaling, it is only the ellipsoid/equivalent sphere model that replicates the actual ODMR response observed in the experiment as illustrated in Fig. 6B and 4B. The ODMR response assuming the hydrodynamic diameter of the ND is smaller than the observations by factor of 2–3 as shown in Fig. 6B.

The results presented above show that the presence of ND itself can perturb analyte sensing in solutions. This is common in microcompartments due to finite size effects, but can also occur in beaker scale samples when the analyte concentration is very low and nanoparticle concentration is high, as illustrated by Eisenthal and coworkers.[50] To account for these bulk depletion effects a modified Langmuir equation is developed that successfully accounts for the influence of compartment size. Finally, not surprisingly, smaller ND exhibit a much larger sensitivity to $Gd^{+3}$ due to the enhanced proximity of the $NV^-$ to the surface. There is a trade-off, however, when probing chemistry in microcompartments, where although the sensitivity of small ND might be larger their overall signal levels are smaller requiring a higher concentration that may in turn lead to bulk phase depletion of the analyte.

# 4. Conclusions

We measured the ODMR response in microdroplets and bulk solutions containing $GdCl_3$. The ODMR response curve is found to have the characteristic shape of a Langmuir adsorption isotherm, which indicates that the $Gd^{+3}$ must adsorb to the surface of the nanodiamond prior to efficient detection. We investigated pH, ligands, salts, and compartment size to understand how each of these solution phase factors impact

$Gd^{+3}$ binding and therefore quantitative measurements of paramagnetic species using ND.

Bulk measurements show that the $Gd^{+3}$ sensing has a strong dependence on pH due to the change in protonation state of the carboxyl groups on the diamond surface. At low pH, when many of the surface sites are protonated, there is a decrease in $Gd^{+3}$ sensitivity. In the presence of zinc chloride there is no loss in sensitivity suggesting that $Zn^{+2}$ does not strongly compete with $Gd^{+3}$ for surface sites at millimolar concentrations. Alternatively, adding Zn-acetate to a $Gd^{+3}$ solution decreases ODMR response indicating that $Gd^{+3}$-acetate complexes do not efficiently bind to the nanodiamond surface. Langmuir models are developed to quantitatively account for how these environmental factors (*i.e.*, pH, [$Gd^{+3}$] depletion and complexation) impact ODMR response as demonstrated in Fig. 3–6.

The ODMR response to $Gd^{+3}$ depends upon nanodiamond shape and size as illustrated in Figs. 3B, 4 and 6. Assuming that ND are spheres using the hydrodynamic diameter under predicts the observed ODMR response to $Gd^{+3}$. Instead, approximating ND shape as ellipsoid or its equivalent sphere captures the $1/r$ scaling of the ODMR response with ND size quantitatively. The photophysical model reveals that this size dependence arises from the higher sensitivity of surface $NV^-$ centers to surface bound $Gd^{+3}$.

$Gd^{+3}$ concentrations as low as 10 nM are measured in bulk solutions. Larger [$Gd^{+3}$] (0.34 μM to 1.5 mM) are detected in droplets. This reduced sensitivity in microdroplets is due to the solution phase depletion, which reduces the limit of detection relative to macroscale solutions. This limitation could potentially be addressed by improving the signal-to-noise ratio, for example through enhancements to the experimental setup or by increasing the NV center density in the nanodiamonds.[62] These improvements would reduce the number of NDs required to probe in-droplet chemistry. This example shows how $Gd^{+3}$ sensitivity is controlled most strongly by the location of the inflection point in the Langmuir adsorption isotherm. Outside of this small concentration range, the ODMR response is not sensitive to changing [$Gd^{+3}$].

The photophysical model developed here is generally applicable to sensing of paramagnetic species that bind to the ND surface. However, any change in surface functionalization or target ion would necessitate new measurements of relevant equilibrium constants governing surface adsorption. The general inhomogeneity in nanodiamond surface functionalization, depending strongly on the synthesis method and often consisting of a variety of oxygen-containing groups,[46] may require a new measurement of $K_{eq}$ for each ND sample. Functionalizing the surface with groups that more efficiently bind $Gd^{+3}$ could significantly increase $K_{eq}$ and decrease the detection limit. Extending this sensing approach to more complex matrices would also necessitate characterization of how each competing species in solution, such as acetate, influence $Gd^{+3}$ binding to the surface, potentially complicating quantitative determination of $Gd^{3+}$ concentration.

In summary, our work expands the foundation of *in situ* nanodiamond-based quantum sensing within microcompartments. Unlike electrospray mass spectrometry (ESI) which is a common method to study reactions in microdroplets, these sensors can serve as nondestructive probes in single droplets which provides more accurate control of droplet size, charge, and concentration.[63] Our results indicate that quantitative measurements of paramagnetic species require a thorough understanding of all solution conditions as even small changes in pH or co-solute concentration can change the ODMR response significantly.

## Author contributions

Project conceptualization: E. K. B., K. R. W., and A. A. nanodiamond experimental set up: Z. J. and A. S. bulk and droplet experiments and data analysis: E. K. B., B. J. W. and K. R. W. photophysical model: E. K. B. and K. R. W. Original draft preparation: E. K. B. and K. R. W. draft editing and review: all authors.

## Conflicts of interest

There are no conflicts of interest to declare.

## Data availability

The data supporting this article have been included as part of the SI.

Supplementary information: the diamond site concentration calculations, a block diagram of the model with a glossery of terms, rate and physical constants, additional details regarding the ellipsoid model, zeta potential and water solvent measurements, and a derivation of the competitive Langmuir model and supporting calibration curves. See DOI: **https://doi.org/10.1039/d5sc04108b**.

## Acknowledgements

The experimental measurements were supported the Laboratory Directed Research and Development program at Lawrence Berkeley National Laboratory. The photophysical and Langmuir models were developed with support from the Director, Office of Energy Research, Office of Basic Energy Sciences, Chemical Sciences Division, Condensed Phase and Interfacial Molecular Sciences Program of the U.S. Department of Energy under contract no. DE-AC02-05CH11231. Dr Brandon Wallace is supported by the William M. Keck Foundation (8959). Prof. Ashok Ajoy acknowledges support from the AFOSR YIP program (FA9550-23-1-0106). The authors thank Emanuel Druga for his help designing microwave antennas, and Dr Olga Shenderova from Adámas Nanotechnologies for providing the nanodiamonds used in this work.

## References

1 H. Wei, E. P. Vejerano, W. Leng, Q. Huang, M. R. Willner, L. C. Marr and P. J. Vikesland, Aerosol Microdroplets Exhibit a Stable pH Gradient, *Proc. Natl. Acad. Sci. U. S. A.*, 2018, **115**(28), 7272–7277, DOI: **10.1073/pnas.1720488115**.

2 H. Hao, I. Leven and T. Head-Gordon, Can Electric Fields Drive Chemistry for an Aqueous Microdroplet?, *Nat. Commun.*, 2022, **13**(1), 280, DOI: **10.1038/s41467-021-27941-x**.

3 C. Chamberlayne and R. N. Zare, Simple Model for the Electric Field and Spatial Distribution of Ions in a Microdroplet, *J. Chem. Phys.*, 2020, **152**(184702), 1–10, DOI: **10.1063/5.0006550**.

4 H. Xiong, J. K. Lee, R. N. Zare and W. Min, Strong Electric Field Observed at the Interface of Aqueous Microdroplets, *J. Phys. Chem. Lett.*, 2020, **11**(17), 7423–7428, DOI: **10.1021/acs.jpclett.0c02061**.

5 Y. Liu, Q. Ge, T. Wang, R. Zhang, K. Li, K. Gong, L. Xie, W. Wang, L. Wang, W. You, X. Ruan, Z. Shi, J. Han, R. Wang, H. Fu, J. Chen, C. K. Chan and L. Zhang, Strong Electric Field Force at the Air/Water Interface Drives Fast Sulfate Production in the Atmosphere, *Chem*, 2024, **10**(1), 330–351, DOI: **10.1016/j.chempr.2023.09.019**.

6 L. Qiu, Z. Wei, H. Nie and R. G. Cooks, Reaction Acceleration Promoted by Partial Solvation at the Gas/Solution Interface, *ChemPlusChem*, 2021, **86**(10), 1362–1365, DOI: **10.1002/cplu.202100373**.

7 D. T. Limmer, A. W. Götz, T. H. Bertram and G. M. Nathanson, Molecular Insights into Chemical Reactions at Aqueous Aerosol Interfaces, *arXiv*, 2023, preprint, arXiv:2306.13811, DOI: **10.48550/arXiv.2306.13811**, accessed 2024-04-30.

8 L. Qiu and R. G. Cooks, Simultaneous and Spontaneous Oxidation and Reduction in Microdroplets by the Water Radical Cation/Anion Pair, *Angew. Chem., Int. Ed.*, 2022, **61**(41), e202210765; *Angew. Chem.*, 2022, **134**, e202210765.

9 J. K. Lee, K. L. Walker, H. S. Han, J. Kang, F. B. Prinz, R. M. Waymouth, H. G. Nam and R. N. Zare, Spontaneous Generation of Hydrogen Peroxide from Aqueous Microdroplets, *Proc. Natl. Acad. Sci. U. S. A.*, 2019, **116**(39), 19294–19298, DOI: **10.1073/pnas.1911883116**.

10 M. D. Torelli, N. A. Nunn and O. A. Shenderova, A Perspective on Fluorescent Nanodiamond Bioimaging, *Small*, 2019, **15**(48), 1902151, DOI: **10.1002/smll.201902151**.

11 L. Rondin, J.-P. Tetienne, T. Hingant, J.-F. Roch, P. Maletinsky and V. Jacques, Magnetometry with Nitrogen-Vacancy Defects in Diamond, *Rep. Prog. Phys.*, 2014, **77**(5), 056503, DOI: **10.1088/0034-4885/77/5/056503**.

12 T. Iwasaki, W. Naruki, K. Tahara, T. Makino, H. Kato, M. Ogura, D. Takeuchi, S. Yamasaki and M. Hatano, Direct Nanoscale Sensing of the Internal Electric Field in Operating Semiconductor Devices Using Single Electron Spins, *ACS Nano*, 2017, **11**(2), 1238–1245, DOI: **10.1021/acsnano.6b04460**.

13 F. Dolde, H. Fedder, M. W. Doherty, T. Nöbauer, F. Rempp, G. Balasubramanian, T. Wolf, F. Reinhard, L. C. L. Hollenberg, F. Jelezko and J. Wrachtrup, Electric-Field Sensing Using Single Diamond Spins, *Nat. Phys.*, 2011, **7**(6), 459–463, DOI: **10.1038/nphys1969**.

14 F. Perona Martínez, A. C. Nusantara, M. Chipaux, S. K. Padamati and R. Schirhagl, Nanodiamond Relaxometry-Based Detection of Free-Radical Species When Produced in Chemical Reactions in Biologically Relevant Conditions, *ACS Sens.*, 2020, **5**(12), 3862–3869, DOI: **10.1021/acssensors.0c01037**.

15 A. O. Sushkov, N. Chisholm, I. Lovchinsky, M. Kubo, P. K. Lo, S. D. Bennett, D. Hunger, A. Akimov, R. L. Walsworth, H. Park and M. D. Lukin, All-Optical Sensing of a Single-Molecule Electron Spin, *Nano Lett.*, 2014, **14**(11), 6443–6448, DOI: **10.1021/nl502988n**.

16 R. D. Allert, K. D. Briegel and D. B. Bucher, Advances in Nano- and Microscale NMR Spectroscopy Using Diamond Quantum Sensors, *Chem. Commun.*, 2022, **58**(59), 8165–8181, DOI: **10.1039/D2CC01546C**.

17 Z. Qin, Z. Wang, F. Kong, J. Su, Z. Huang, P. Zhao, S. Chen, Q. Zhang, F. Shi and J. Du, In Situ Electron Paramagnetic Resonance Spectroscopy Using Single Nanodiamond Sensors, *Nat. Commun.*, 2023, **14**(1), 6278, DOI: **10.1038/s41467-023-41903-5**.

18 J. Holzgrafe, Q. Gu, J. Beitner, D. M. Kara, H. S. Knowles and M. Atatüre, Nanoscale NMR Spectroscopy Using Nanodiamond Quantum Sensors, *Phys. Rev. Appl.*, 2020, **13**(4), 044004, DOI: **10.1103/PhysRevApplied.13.044004**.

19 T. F. Segawa and R. Igarashi, Nanoscale Quantum Sensing with Nitrogen-Vacancy Centers in Nanodiamonds – A Magnetic Resonance Perspective, *Prog. Nucl. Magn. Reson. Spectrosc.*, 2023, **134–135**, 20–38, DOI: **10.1016/j.pnmrs.2022.12.001**.

20 R. D. Allert, F. Bruckmaier, N. R. Neuling, F. A. Freire-Moschovitis, K. S. Liu, C. Schrepel, P. Schätzle, P. Knittel, M. Hermans and D. B. Bucher, Microfluidic Quantum Sensing Platform for Lab-on-a-Chip Applications, *Lab Chip*, 2022, **22**(24), 4831–4840, DOI: **10.1039/D2LC00874B**.

21 M. A. Eatoo and H. Mishra, Busting the Myth of Spontaneous Formation of $H_2O_2$ at the Air–Water Interface: Contributions of the Liquid–Solid Interface and Dissolved Oxygen Exposed, *Chem. Sci.*, 2024, **15**(9), 3093–3103, DOI: **10.1039/D3SC06534K**.

22 C. J. Chen and E. R. Williams, Are Hydroxyl Radicals Spontaneously Generated in Unactivated Water Droplets?, *Angew. Chem., Int. Ed.*, 2024, **63**(51), e202407433, DOI: **10.1002/anie.202407433**.

23 V. Radu, J. C. Price, S. J. Levett, K. K. Narayanasamy, T. D. Bateman-Price, P. B. Wilson and M. L. Mather, Dynamic Quantum Sensing of Paramagnetic Species Using Nitrogen-Vacancy Centers in Diamond, *ACS Sens.*, 2020, **5**(3), 703–710, DOI: **10.1021/acssensors.9b01903**.

24 V. Yu. Osipov, D. W. Boukhvalov and K. Takai, Gadolinium Ion Bonding on the Surface of Carboxylated Detonation Nanodiamond in Terms of Magnetochemistry and Density Functional Theory, *Mendeleev Commun.*, 2020, **30**(4), 436–438, DOI: **10.1016/j.mencom.2020.07.010**.

25 F. C. Ziem, N. S. Götz, A. Zappe, S. Steinert and J. Wrachtrup, Highly Sensitive Detection of Physiological Spins in a Microfluidic Device, *Nano Lett.*, 2013, **13**(9), 4093–4098, DOI: **10.1021/nl401522a**.

26 S. Iyer, C. Yao, O. Lazorik, M. S. Bin Kashem, P. Wang, G. Glenn, M. Mohs, Y. Shi, M. Mansour, E. Henriksen, K. Murch, S. Mukherji and C. Zu, Optically-Trapped-

Nanodiamond Relaxometric Detection of Nanomolar Paramagnetic Spins in Aqueous Environments, *Phys. Rev. Appl.*, 2024, **22**(6), 064076, DOI: 10.1103/PhysRevApplied.22.064076.

27 E. K. Brown, G. Rovelli and K. R. Wilson, pH Jump Kinetics in Colliding Microdroplets: Accelerated Synthesis of Azamonardine from Dopamine and Resorcinol, *Chem. Sci.*, 2023, **14**(23), 6430–6442, DOI: 10.1039/D3SC01576A.

28 J. F. Davies, Mass, Charge, and Radius of Droplets in a Linear Quadrupole Electrodynamic Balance, *Aerosol Sci. Technol.*, 2019, **53**(3), 309–320, DOI: 10.1080/02786826.2018.1559921.

29 M. I. Jacobs, J. F. Davies, L. Lee, R. D. Davis, F. Houle and K. R. Wilson, Exploring Chemistry in Microcompartments Using Guided Droplet Collisions in a Branched Quadrupole Trap Coupled to a Single Droplet, Paper Spray Mass Spectrometer, *Anal. Chem.*, 2017, **89**(22), 12511–12519, DOI: 10.1021/acs.analchem.7b03704.

30 M. D. Willis, G. Rovelli and K. R. Wilson, Combining Mass Spectrometry of Picoliter Samples with a Multicompartment Electrodynamic Trap for Probing the Chemistry of Droplet Arrays, *Anal. Chem.*, 2020, **92**(17), 11943–11952, DOI: 10.1021/acs.analchem.0c02343.

31 H. Nakagawa and T. Oyama, Molecular Basis of Water Activity in Glycerol–Water Mixtures, *Front. Chem.*, 2019, **7**, 731, DOI: 10.3389/fchem.2019.00731.

32 Functionalized Red Fluorescent Nanodiamond. Adámas Nano, https://www.adamasnano.com.

33 S. Eldemrdash, G. Thalassinos, A. Alzahrani, Q. Sun, E. Walsh, E. Grant, H. Abe, T. L. Greaves, T. Ohshima, P. Cigler, P. Matějíček, D. A. Simpson, A. D. Greentree, G. Bryant, B. C. Gibson and P. Reineck, Fluorescent HPHT Nanodiamonds Have Disk- and Rod-like Shapes, *Carbon*, 2023, **206**, 268–276, DOI: 10.1016/j.carbon.2023.02.018.

34 *Functionalized Red Fluorescent Nanodiamond*, Adamas Nanotechnologies, Inc. https://www.adamasnano.com/functionalized-red-fnd-information, accessed 2025-01-15.

35 A. Sarkar, Z. R. Jones, M. Parashar, E. Druga, A. Akkiraju, S. Conti, P. Krishnamoorthi, S. Nachuri, P. Aman, M. Hashemi, N. Nunn, M. D. Torelli, B. Gilbert, K. R. Wilson, O. A. Shenderova, D. Tanjore and A. Ajoy, High-Precision Chemical Quantum Sensing in Flowing Monodisperse Microdroplets, *Sci. Adv.*, 2024, **10**(50), eadp4033, DOI: 10.1126/sciadv.adp4033.

36 S. K. R. Singam, J. Motylewski, A. Monaco, E. Gjorgievska, E. Bourgeois, M. Nesládek, M. Giugliano and E. Goovaerts, Contrast Induced by a Static Magnetic Field for Improved Detection in Nanodiamond Fluorescence Microscopy, *Phys. Rev. Appl.*, 2016, **6**(6), 064013, DOI: 10.1103/PhysRevApplied.6.064013.

37 J.-P. Tetienne, T. Hingant, L. Rondin, A. Cavaillès, L. Mayer, G. Dantelle, T. Gacoin, J. Wrachtrup, J.-F. Roch and V. Jacques, Spin Relaxometry of Single Nitrogen-Vacancy Defects in Diamond Nanocrystals for Magnetic Noise Sensing, *Phys. Rev. B: Condens. Matter Mater. Phys.*, 2013, **87**(23), 235436, DOI: 10.1103/PhysRevB.87.235436.

38 Y. Dumeige, M. Chipaux, V. Jacques, F. Treussart, J.-F. Roch, T. Debuisschert, V. M. Acosta, A. Jarmola, K. Jensen, P. Kehayias and D. Budker, Magnetometry with Nitrogen-Vacancy Ensembles in Diamond Based on Infrared Absorption in a Doubly Resonant Optical Cavity, *Phys. Rev. B: Condens. Matter Mater. Phys.*, 2013, **87**(15), 155202, DOI: 10.1103/PhysRevB.87.155202.

39 N. Nunn, M. Torelli, G. McGuire and O. Shenderova, Nanodiamond: A High Impact Nanomaterial, *Curr. Opin. Solid State Mater. Sci.*, 2017, **21**(1), 1–9, DOI: 10.1016/j.cossms.2016.06.008.

40 P. Reineck, L. F. Trindade, J. Havlik, J. Stursa, A. Heffernan, A. Elbourne, A. Orth, M. Capelli, P. Cigler, D. A. Simpson and B. C. Gibson, Not All Fluorescent Nanodiamonds Are Created Equal: A Comparative Study, *Part. Part. Syst. Charact.*, 2019, **36**(3), 1900009, DOI: 10.1002/ppsc.201900009.

41 Wolfram Research, Inc. Mathematica, 2022.

42 T. Fujisaku, R. Tanabe, S. Onoda, R. Kubota, T. F. Segawa, F. T.-K. So, T. Ohshima, I. Hamachi, M. Shirakawa and R. Igarashi, pH Nanosensor Using Electronic Spins in Diamond, *ACS Nano*, 2019, **13**(10), 11726–11732, DOI: 10.1021/acsnano.9b05342.

43 T. Rendler, J. Neburkova, O. Zemek, J. Kotek, A. Zappe, Z. Chu, P. Cigler and J. Wrachtrup, Optical Imaging of Localized Chemical Events Using Programmable Diamond Quantum Nanosensors, *Nat. Commun.*, 2017, **8**(1), 14701, DOI: 10.1038/ncomms14701.

44 S. F. Schultz, T. Gisler, M. Borkovec and H. Sticher, Surface Charge on Functionalized Latex Spheres in Aqueous Colloidal Suspensions, *J. Colloid Interface Sci.*, 1994, **164**, 88–98.

45 S. E. Burke and C. J. Barrett, Acid–Base Equilibria of Weak Polyelectrolytes in Multilayer Thin Films, *Langmuir*, 2003, **19**(8), 3297–3303, DOI: 10.1021/la026500i.

46 F. Gareeva, N. Petrova, O. Shenderova and A. Zhukov, Electrokinetic Properties of Detonation Nanodiamond Aggregates in Aqueous KCl Solutions, *Colloids Surf., A*, 2014, **440**, 202–207.

47 A. M. Panich, A. I. Shames, N. A. Sergeev, V. Yu. Osipov, A. E. Alexenskiy and A. Ya Vul', Magnetic Resonance Study of Gadolinium-Grafted Nanodiamonds, *J. Phys. Chem. C*, 2016, **120**(35), 19804–19811, DOI: 10.1021/acs.jpcc.6b05403.

48 S. Iyer, C. Yao, O. Lazorik, P. Wang, G. Glenn, M. Mohs, Y. Shi, M. Mansour, E. Henriksen, K. Murch, S. Mukherji and C. Zu, Optically-Trapped Nanodiamond-Relaxometry Detection of Nanomolar Paramagnetic Spins in Aqueous Environments, *arXiv*, 2024, preprint, arXiv:2401.17372, DOI: 10.48550/arXiv.2401.17372, accessed 2024-04-29.

49 Y. Liu, Is the Free Energy Change of Adsorption Correctly Calculated?, *J. Chem. Eng. Data*, 2009, **54**(7), 1981–1985, DOI: 10.1021/je800661q.

50 H. Wang, E. C. Y. Yan, Y. Liu and K. B. Eisenthal, Energetics and Population of Molecules at Microscopic Liquid and Solid Surfaces, *J. Phys. Chem. B*, 1998, **102**(23), 4446–4450, DOI: 10.1021/jp980491y.

51 W. T. S. Cole, H. Wei, S. C. Nguyen, C. B. Harris, D. J. Miller and R. J. Saykally, Dynamics of Micropollutant Adsorption to Polystyrene Surfaces Probed by Angle-Resolved Second

Harmonic Scattering, *J. Phys. Chem. C*, 2019, **123**(23), 14362–14369, DOI: **10.1021/acs.jpcc.9b01146**.

52 M. Černík, M. Borkovec and J. C. Westall, Affinity Distribution Description of Competitive Ion Binding to Heterogeneous Materials, *Langmuir*, 1996, **12**(25), 6127–6137, DOI: **10.1021/la960008f**.

53 J. P. Gustafsson, Visual MINTEQ, **https://vminteq.com/**.

54 K. Wilson and A. Prophet, Chemical Kinetics in Microdroplets, *Annu. Rev. Phys. Chem.*, 2024, **75**, 185–208, DOI: **10.1146/annurev-physchem-052623120718**.

55 A. M. Prophet, D. T. Limmer and K. R. Wilson, Surfactant Control of Interfacial Reaction Rates in Aqueous Microdroplets, *Phys. Chem. Chem. Phys.*, 2025, **27**(31), 16465–16478, DOI: **10.1039/D5CP01573A**.

56 A. Bain, L. Lalemi, N. Croll Dawes, R. E. H. Miles, A. M. Prophet, K. R. Wilson and B. R. Bzdek, Surfactant Partitioning Dynamics in Freshly Generated Aerosol Droplets, *J. Am. Chem. Soc.*, 2024, **146**(23), 16028–16038, DOI: **10.1021/jacs.4c03041**.

57 M. Pelliccione, B. A. Myers, L. M. A. Pascal, A. Das and A. C. Bleszynski Jayich, Two-Dimensional Nanoscale Imaging of Gadolinium Spins via Scanning Probe Relaxometry with a Single Spin in Diamond, *Phys. Rev. Appl.*, 2014, **2**(5), 054014, DOI: **10.1103/PhysRevApplied.2.054014**.

58 K.-M. C. Fu, C. Santori, P. E. Barclay and R. G. Beausoleil, Conversion of Neutral Nitrogen-Vacancy Centers to Negatively Charged Nitrogen-Vacancy Centers through Selective Oxidation, *Appl. Phys. Lett.*, 2010, **96**(12), 121907, DOI: **10.1063/1.3364135**.

59 M. V. Hauf, B. Grotz, B. Naydenov, M. Dankerl, S. Pezzagna, J. Meijer, F. Jelezko, J. Wrachtrup, M. Stutzmann, F. Reinhard and J. A. Garrido, Chemical Control of the Charge State of Nitrogen-Vacancy Centers in Diamond, *Phys. Rev. B: Condens. Matter Mater. Phys.*, 2011, **83**(8), 081304, DOI: **10.1103/PhysRevB.83.081304**.

60 C. Santori, P. E. Barclay, K.-M. C. Fu and R. G. Beausoleil, Vertical Distribution of Nitrogen-Vacancy Centers in Diamond Formed by Ion Implantation and Annealing, *Phys. Rev. B: Condens. Matter Mater. Phys.*, 2009, **79**(12), 125313, DOI: **10.1103/PhysRevB.79.125313**.

61 J. D. Rindelaub, R. L. Craig, L. Nandy, A. L. Bondy, C. S. Dutcher, P. B. Shepson and A. P. Ault, Direct Measurement of pH in Individual Particles via Raman Microspectroscopy and Variation in Acidity with Relative Humidity, *J. Phys. Chem. A*, 2016, **120**(6), 911–917, DOI: **10.1021/acs.jpca.5b12699**.

62 C. Laube, T. Oeckinghaus, J. Lehnert, J. Griebel, W. Knolle, A. Denisenko, A. Kahnt, J. Meijer, J. Wrachtrup and B. Abel, Controlling the Fluorescence Properties of Nitrogen Vacancy Centers in Nanodiamonds, *Nanoscale*, 2019, **11**(4), 1770–1783, DOI: **10.1039/c8nr07828a**.

63 G. Rovelli, M. I. Jacobs, M. D. Willis, R. J. Rapf, A. M. Prophet and K. R. Wilson, A Critical Analysis of Electrospray Techniques for the Determination of Accelerated Rates and Mechanisms of Chemical Reactions in Droplets, *Chem. Sci.*, 2020, **11**(48), 13026–13043, DOI: **10.1039/D0SC04611F**.